Applied Catalysis B: Environmental 268 (2020) 118745

Contents lists available at ScienceDirect

Applied Catalysis B: Environmental

journal homepage: www.elsevier.com/locate/apcatb

Efficient magnetic hybrid ZnO-based photocatalysts for visible-light-driven removal of toxic cyanobacteria blooms and cyanotoxins

Albert Serrà[a,*], Petai Pip[a,b,c], Elvira Gómez[d,e], Laetitia Philippe[a]

[a] Empa, Swiss Federal Laboratories for Materials Science and Technology, Laboratory for Mechanics of Materials and Nanostructures, Feuerwerkerstrasse 39, CH-3602, Thun, Switzerland
[b] Laboratory for Mesoscopic Systems, Department of Materials, ETH Zurich, 8093, Zurich, Switzerland
[c] Laboratory for Multiscale Materials Experiments, Paul Scherrer Institute, 5232, Villigen PSI, Switzerland
[d] Grup d'Electrodeposició de Capes Primes i Nanoestructures (GE-CPN), Departament de Ciència de Materials i Química Física, Universitat de Barcelona, Martí i Franquès, 1, E-08028, Barcelona, Catalonia, Spain
[e] Institute of Nanoscience and Nanotechnology (IN^{2}UB), Universitat de Barcelona, Barcelona, Catalonia, Spain

ARTICLE INFO

Keywords:
Photocatalysis
ZnO-based photocatalysts
Microalgae
Cyanobacteria blooms
Cyanotoxins degradation

ABSTRACT

A hybrid magnetic-ZnO-based photocatalyst platform is designed for the efficient and simultaneous sunlight-driven photoremoval of cyanobacteria and mineralization of cyanotoxins (anatoxin-A). The photocatalyst killing ability was evaluated against two types of microalgae with different morphology and toxicity, *Spirulina platensis paracas* and *Anabaena flos-aquae*. The hybrid photocatalyst Ni@ZnO@ZnS-*Spirulina* was synthetized by means of a multistep process using *Spirulina* as biotemplate. The effects of reactor geometry, magnetic actuation, and concordant architecture on photokilling ability were tested. Moreover, the prepared photocatalysts were demonstrated to be effective for the anatoxin-A degradation under artificial sunlight. In the interest of reducing waste content and optimizing resources, photocatalyst recycling after their useful lifetime has ended is proposed through the fabrication of microalgal biofuel-pellets. This inexpensive circular process involves multi-functional algae-based photocatalysts applied to the simultaneous destruction of algae blooms and cyanotoxins and then recycled to close the circle through cultivating biotemplates.

1. Introduction

The ongoing occurrence of harmful algal blooms (HABs) poses a major risk to water resources and evidences the continuing eutrophication of global aquatic ecosystems. HAB formation is caused by multiple difficult to individualize factors that severely modify water conditions to cause abnormal growth of certain species of algae [1–3]. In addition to being driven by anthropological and eutrophication activities such as water pollution, HAB formation is promoted by the global temperature increase and is therefore expected to become more widespread in the future. HABs can occur under a wide range of environmental conditions but are most often observed in (sub)tropical regions [4,5]. Importantly, 25 %–75 % of algal blooms are toxic, producing a wide range of toxins and toxic phytoplankton that adversely affect the health of humans, animals, and aquatic biota. HABs can even change the odor, taste, or color of water, which generally turns red or brown. However, these changes are not always observed [6–8]. Cyanobacteria are ubiquitous photosynthetic prokaryotes in natural terrestrial and aquatic environments, being capable of growth in adverse environments ranging from deserts to ice-cold waters. Consequently, cyanobacteria blooms and cyanotoxins are commonly found worldwide, e.g., in Europe, Australia, and North America as well as the high-alpine waters of Switzerland [9–12]. Thus, toxic cyanobacteria blooms are possibly the main HABs because of their formation frequency, global presence, production of a wide range of potent toxins (known as cyanotoxins), and the corresponding reduction in oxygen levels and release of ammonia, which can dramatically affect aquatic biota, especially fish [1–3].

Cyanotoxins exert strong adverse effects on humans and animals, and are therefore one of the primary serious risks associated with water resources, causing liver damage, respiratory paralysis, or other fatal conditions even at extremely low concentrations. In general, humans are mainly exposed to cyanotoxins through the ingestion of drinking water or during recreational water activities [13–16]. Based on their adverse effects on humans/animals, cyanotoxins are mainly grouped into hepatotoxins (comprising microcystins, nodularins, and clyndospermopsin), which can cause dramatic liver damage; neurotoxins (comprising anatoxin-A, anatoxin-A(s), saxitoxins, β-*N*-methylamino-L-alanine, and other neurotoxins), which cause death via respiratory

* Corresponding author.
E-mail address: albert.serraramos@empa.ch (A. Serrà).

https://doi.org/10.1016/j.apcatb.2020.118745
Received 17 December 2019; Received in revised form 31 January 2020; Accepted 8 February 2020
Available online 09 February 2020

paralysis in humans or asphyxiation in animals; cyto-toxins (comprising aplysiatoxins, debromoaplysiatoxins, lyngbyatoxins, and cylindrospermopsin), which cause cell damage that affects several organs such as the small intestine or adrenal glands; and dermatoxins, which cause skin irritation [13–16].

In view of the above adverse effects, the World Health Organization (WHO) and the US Environmental Protection Agency (EPA) have established provisional toxin levels in drinking water. For example, WHO recommends that microcystin-LR (hepatotoxin) concentrations in drinking and recreational water should be lower than 1 and 20 μg L^{-1}, respectively. Similarly, EPA recommends that microcystin-LR (hepatotoxin) and anatoxin-A (neurotoxin) concentrations should be lower than 1.6 and 6 μg L^{-1}, respectively. Local, national, state, and supra-state regulations and guidelines for water quality generally incorporate the cyanotoxin control for both drinking and recreational water [17–20]. However, conventional treatments applied in drinking water treatment plants cannot totally eliminate extracellular cyanotoxins, being only suited for the elimination of a very limited number of them. For example, coagulation, flocculation, sedimentation, filtration, flotation, and chlorination cannot effectively remove anatoxin-A [21–24]. Consequently, the exploration of advanced oxidation (e.g., photocatalysis and photo-Fenton) processes for the effective elimination of cyanotoxins of all types, especially anatoxin-A is a task of high significance. Among these methods, sunlight-driven photocatalysis has been recognized as an efficient, clean, and inexpensive strategy for the mineralization of various persistent organic pollutants and the deactivation of microorganisms in wastewater [25–31].

Herein, we develop an effective multifunctional hybrid magnetic ZnO-based photocatalyst platform focused on non-toxic *Spirulina* cyanobacteria for the simultaneous sunlight-driven removal of cyanobacteria blooms and mineralization of cyanotoxins (in particular, anatoxin-A). The employed photocatalyst design aims to both enhance decontamination processes and integrate a cleaner production concept. In doing so, we explore the photocatalyst recycling potential via the incorporation of a green circular process to produce microalgal pellets and microalgal cultivation media and consequently prevent the generation of any types of residue. In this regard, the synthesis of Ni@ZnO@ZnS-*Spirulina* hybrid photocatalysts is optimized using a simple multi-step process based on biotemplating, chemical deposition, and sulfidation. Additionally, we explore the photokilling activity of sunlight irradiation and magnetic actuation to remove cyanobacterial blooms and photo-mineralize cyanotoxins – in particular, anatoxin-A. Two types of microalgae – *Spirulina platensis paracas* and Anabaena *flos-aquae* – were used to test the photokilling activity and effects of reactor geometry and photocatalyst architecture. The magnetic actuation and reusability were also explored. After the photocatalyst had reached its lifetime, the hybrid platform was employed for the production of microalgal pellets (i.e., non-woody biofuels) to obtain energy via combustion, which mainly generates carbon dioxide and microalgal ashes. Finally, to reduce the volume of residue generated during the whole process, microalgal ashes was used as a supplement for the production of inexpensive microalgal cultivation media. Importantly, the high cost of cultivation media is one of the main limiting parameters in the cultivation and commercialization of microalgae. Additionally, the cultivation of new *Spirulina* microalgae enabled the recycling of microalgal ash, fixation of CO_2 released during the mineralization of anatoxin-A and the combustion of microalgae pellets, and enable the fabrication of more multifunctional Ni@ZnO@ZnS-*Spirulina* hybrid photocatalysts to result in a green circular process that produces nearly no residue.

2. Experimental

2.1. Synthesis and characterization of Ni@ZnO@ZnS hybrid photocatalysts

2.1.1. Synthesis of Ni@ZnO@ZnS hybrid photocatalysts

Spirulina platensis paracas cyanobacteria—a helical microalga—were selected as the skeleton for the biotemplating process. The microalgae were cultivated in a 30 L glass tank at 30 °C using Zarrouk's medium, natural sunlight irradiation (average light intensity of 1350 ± 450 lx), intermittent mechanical agitation (80 rpm; 30 min-15 min on-off cycles), and air bubbling (15 min–60 min on-off cycles). The pH was maintained at a value of 10.

Onion-like Ni@ZnO@ZnS hybrid microalgae were synthesized using a scalable multi-step biotemplating process (Fig. 1a), based on:

(i) Microalgae fixation: To prevent fragmentation, microalgae were resuspended in 10 % glutaraldehyde (#G5882, Sigma-Aldrich) in phosphate-buffered saline (PBS; 0.01 M phosphate buffer, 0.0027 M KCl, and 0.137 M NaCl; pH 7.4) over 6 h at 25 °C.
(ii) Palladium catalyzation: To prepare the microalgae surface for the posterior metallization process, the fixed microalgae were filtered and resuspended in a palladium catalyzation bath for 35 min at 35 °C. Palladium catalyzation, also known as the sensitizing-activation method, is one of the pivotal steps in the Ni electroless process, especially on non-conductive substrates. Fixed microalgae were dispersed in the palladium catalyzation bath, consisting of stannous chloride and palladium chloride colloidally dispersed in a dilute solution of sulfuric acid and sodium chloride, leading to the formation of palladium nuclei on the microalgae, which are capable of catalytically depositing Ni from the nickel electroless bath.
(iii) Nickel electroless deposition: To form a nickel shell on the microalgae, producing magnetic Ni hybrid microalgae, the catalytic microalgae were filtered, washed with HCl (x3), PBS (x2), and deionized water, and resuspended in nickel electroless deposition bath for 45 min at 70 °C. The nickel electroless bath consisted of 0.2 M sodium citrate tribasic dehydrate (Sigma-Aldrich, > 99 %), 0.1 M $NiSO_4{\cdot}6H_2O$ (Sigma-Aldrich, > 99 %), and 0.05 M borane dimethylamine complex (Sigma-Aldrich, 97 %).
(iv) Zinc oxide chemical deposition: The nickel hybrid microalgae were magnetically collected, washed with deionized water (x5), and resuspended in a zinc oxide chemical deposition bath for 8 min at 70 °C to form a thin ZnO layer, resulting in an onion-like Ni@ZnO-Spirulina hybrid microstructure. The ZnO chemical deposition bath consisted of 0.01 M $Zn(NO_3)_2$ (Sigma-Aldrich, > 99 %) and 0.01 M borane dimethylamine complex.
(v) Sulfidation: The microstructures were magnetically collected and resuspended in an aqueous solution of 30 mM thioacetamide (Sigma-Aldrich, 98 %) for 4 h at 85 °C to form a ZnS shell, resulting in an onion-like Ni@ZnO@ZnS-*Spirulina* microstructure.

2.1.2. Characterization of Ni@ZnO@ZnS hybrid photocatalysts

The Ni@ZnO@ZnS hybrid microalgae were characterized in terms of morphological, architectural and elemental composition characterization using FE-SEM microscope (Hitachi S-4800) equipped with an energy-dispersive X-ray spectroscopy detector. The Brunauer–Emmett–Teller (BET) surface areas were measured from N_2 adsorption-desorption isotherms at 77 K using a Micrometrics Tristar-II. The crystal phases were determined by X-ray diffraction (XRD, Bruker D8 Discovery diffractometer) in the Bragg–Brentano configuration with Cu K_α radiation. Magnetic properties were measured at 300 K with superconducting quantum interference device vibrating sample magnetometry (SQUID-VSM, Quantum design MPMS3). Microalgae optical and electronic properties were characterized by UV–vis spectroscopy (PerkinElmer Lambda 900 UV spectrophotometer).

2.2. Antimicrobial activity of Ni@ZnO@ZnS hybrid photocatalysts

The antibacterial activity of hybrid microalgae was evaluated against two different species of green-blue microalgae: (i) *Spirulina platensis paracas* cyanobacteria, which are popularly used as an alimentary supplement (non-toxic microalgae) [32–34]; and (ii) Anabaena *flos-aquae* cyanobacteria, which produce anatoxins (microcystin)

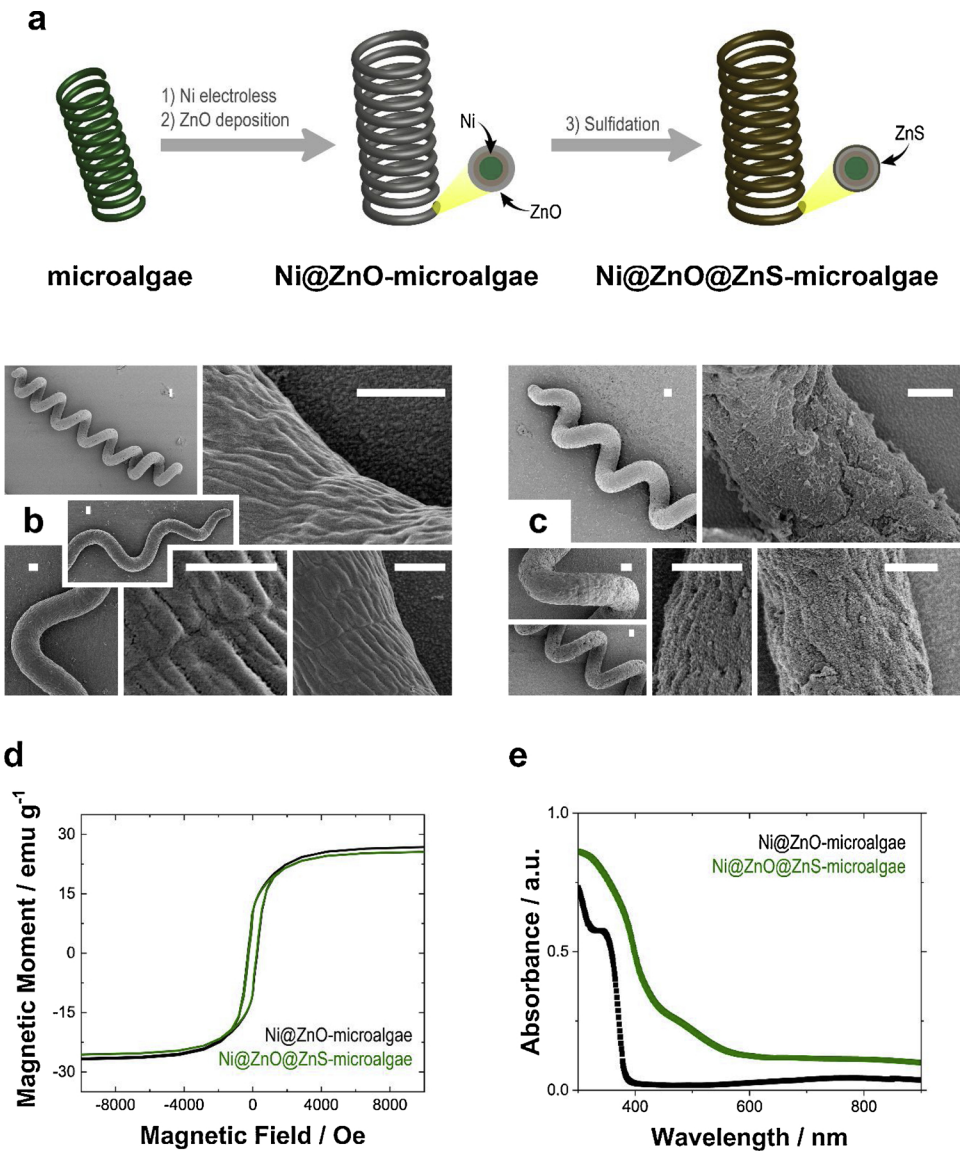

Fig. 1. (a) Schematic representation of the biotemplating multi-step process for synthesizing Ni@ZnO@ZnS-*Spirulina* hybrid photocatalysts. The FE-SEM micrographs of (b) Ni@ZnO-*Spirulina* and (c) Ni@ZnO@ZnS-*Spirulina* hybrid photocatalysts. Scale bar: 2 μm. (d) The hysteresis loop (M-H curves) of Ni@ZnO-*Spirulina* and Ni@ZnO@ZnS-*Spirulina* hybrid photocatalysts. (e) The UV–vis DRS absorption spectra of Ni@ZnO-*Spirulina* and Ni@ZnO@ZnS-*Spirulina* hybrid photocatalysts.

[35–37]. *Spirulina platensis paracas* and Anabaena *flos-aquae* were respectively cultivated in Zarrouk's and ASM medium, all under natural sunlight irradiation (average light intensity of 1350 ± 450 lx), intermittent mechanical agitation (80 rpm; 30 min–15 min on-off cycles), and air bubbling (15 min–60 min on-off cycles). In brief, for antimicrobial activity assessment, 250 mL of each microalgae culture (initial concentration ~100 ± 10 × 10^3 microalgae mL^{-1}) was combined with 150 mg of Ni@ZnO@ZnS hybrid microalgae in dark conditions and kept in the dark for 30 min prior to photo-irradiation. A 75 W Xe lamp (light intensity of 680 ± 10 lx) was used as a simulated solar light source, with UV irradiation ($\lambda < 400$ nm) removed by a 400 nm UV cut-off filter. The suspensions were then irradiated with this artificial sunlight for 80 min to determine the antibacterial activity of Ni@ZnO@ZnS hybrid microalgae photocatalysts. During the irradiation period, the suspensions were also subjected to a 400 Oe rotatory magnetic field at 0, 10, 20 and 30 Hz (magnetic stirrer RH digital – IKA®). All experiments were conducted at room temperature (25 ± 0.2 °C). At given timepoints during the experiment, 100 μL of the suspension was collected and analyzed with a hemacytometer. Each experiment was repeated six times to ensure accuracy. Additionally, microalgae biomass growth was determined over an eight-day period in appropriate media containing 0.6 g L^{-1} of Ni@ZnO@ZnS hybrid microalgae. Each day, three 20 mL samples were extracted from each microalgae cultivation tank and filtered through pre-weighed GF/F Whatman® glass microfiber filters (WHA1825021, Sigma-Aldrich), which were dried in an oven at 40 °C and then weighed. Biomass production was calculated as mg L^{-1}.

2.3. Photocatalytic activity of Ni@ZnO@ZnS hybrid photocatalysts

The photocatalytic activity of Ni@ZnO@ZnS hybrid microalgae against cyanotoxins was evaluated using a solution containing 5 ppm of (±)-anatoxin-A fumarate (Hello Bio Limited, > 99 %) as a model cyanotoxin. Briefly, 2 mg of Ni@ZnO or Ni@ZnO@ZnS hybrid microalgae were suspended in 5 mL of the cyanotoxin solution in the dark, and kept in the darkroom for 90 min at 25 °C to establish an adsorption-desorption equilibrium. A 75 W Xe lamp setup (light intensity of 680 ± 10 lx) was used as a simulated solar light source. To determine photocatalytic activity, the pollutant solutions were exposed to the irradiation and subjected to a 400 Oe magnetic at 0, 10, 20 and 30 Hz (magnetic stirrer RH digital – IKA®). Photodegradation was measured

as the temporal evolution of the reduction in (±)-anatoxin-A concentration, determined using an ultra-high-performance liquid chromatography (UHPLC) system (Accela; Thermo Fisher Scientific). The separation was performed in a Kinetex HILIC column – 100 mm × 2.1 mm i.d., 2.6 µm particle size – (Phenomenex), using a gradient elution of solvent A and solvent B. Solvent A consisted of 95 % (v/v) of acetonitrile + 5 % (v/v) of an aqueous solution, containing 2 mM of ammonium formate and 3.6 mM of formic acid. Solvent B consisted of an aqueous solution of 2 mM of ammonium formate and 3.6 mM of formic acid. The flow rate was 200 µL min^{-1} and the column temperature was held at 25 °C. An isocratic gradient, where the mobile phase was 85 % (v/v) of solvent A and 15 % (v/v) of solvent B, was used. Mobile phases were filtered using 0.22 µm nylon membrane filters (Whatman), and sample extracts were filtered through 0.22 µm pore size Ultrafree-MC centrifuge filters (Millipore). The UHPLC system was coupled to a triple quadrupole mass spectrometer (TSQ Quantum Ultra AM, Thermo Fisher Scientific), equipped with a heated electrospray ionization source (HESI-I). Nitrogen was used as a sheath gas, ion sweep gas and auxiliary gas at flow rates of 60, 20 and 40 a.u. (arbitrary units), respectively. The ion transfer tube temperature was set at 350 °C and electrospray voltage at + 4.5 kV. Argon was used as a collision gas at 1.5 mTorr. Xcalibur software (version 2.0; Thermo Fisher Scientific) was used to control the LC/MS system and to process data. Mineralization was determined by comparing the initial total organic carbon (TOC) content with its temporal evolution over 180 min; TOC content was measured by a tubular flow microreactor (TOC-V_{CSH}, Shimadzu) with a high-sensibility column operated at 680 °C, using the high-temperature combustion method on a catalyst (Pt-Al_2O_3), and with a stream of hydrocarbon-free air to oxidize the organic carbon. Finally, the photocatalysts were magnetically collected, washed dried at 40 °C, and reused for five consecutive mineralization runs with the mineralization determined after each recycling experiment.

2.4. Recyclability of Ni@ZnO@ZnS hybrid photocatalysts

After their effective lifetime, the photocatalysts were recycled through fabricating microalgae pellets using a single pelletizer machine. Based on the UNE-EN ISO 18134-2 standard, the humidity content of microalgae pellets was determined with a balance (accuracy ± 0.0001 g) and an oven at 105 °C. The calorific power of the microalgae pellets was determined using an IKA® calorimeter C5000. Pellets were combusted in a Heraeus M110 Muffel oven (constant temperature of 900 °C) to obtain ashes and the ashes were used as a supplement for the cultivation of more *Spirulina platensis paracas* microalgae. Microalgal biomass growth while supplementing with microalgal ashes was determined using the procedure mentioned above.

3. Results and discussion

3.1. Synthesis and characterization of Ni@ZnO@ZnS hybrid photocatalysts

The synthesis of microorganism-metal/semiconductor hybrids based on the biotemplating approach recently has been demonstrated as an easy method to mass produce and fabricate new complex biomimetic architectures [38–41]. This approach is of interest because it avoids the production limitations of the main physical methods of manufacturing artificial bio-inspired templates or bio-inspired materials in terms of the amount of material that can be produced and the difficulties of the scalability processes. The biotemplating approach also provides the possibility of reusing hybrids at the end of their useful lifetimes [41]. For example, they can be reused as raw materials for new applications (e.g., the production of biomass), and this would allow the development of competitive materials that are closer to the principles of green chemistry and circular chemistry, thereby promoting a circular economy process with minimal residues.

In this study, the *paracas* strain of *Spirulina* was selected as the biotemplate skeleton due to its extended helical shape (Fig. S1) (length of 50–130 µm and diameter of 5–9 µm). This can be beneficial for both the photo-antimicrobial activity to kill toxic cyanobacteria and the photocatalytic activity to mineralize cyanotoxins in terms of microorganism-photocatalyst interaction, light tapping, and pollutant adsorption. The shape and dimensions of the microalgae were determined by analyzing 30 different optical micrographs (i.e., more than 90 microalgae). Note that the *Spirulina* microalgae are non-toxic and inexpensive, and they can grow in both alkaline and saline media. In addition, they can be cultivated in adverse conditions, such as in wastewater, which provides an excellent, inexpensive strategy for the mass production of 3D hybrid helices.

Onion-like Ni@ZnO@ZnS-microalgae hybrids were synthesized easily by using a simple and scalable biotemplating multi-step process based on the sequential combination of Ni electroless, the chemical deposition of ZnO, and the sulfidation processes (Fig. 1a) [41]. The detailed morphology and the ferromagnetic and opto-electronic properties of the onion-like helical hybrids are presented in Fig. 1. As shown in Fig. 1b and c, after the biotemplating multi-step process, continuous and homogeneous coatings of ZnO and ZnS are obtained, well-defined 3D helical springs of Ni@ZnO-*Spirulina* and Ni@ZnO@ZnS-*Spirulina* hybrids are formed. The dimensions of the hybrid micro-helices are identical to the dimensions of the *Spirulina* skeleton, i.e., the length ranged between 50–130 µm, the diameter was about 15–25 µm, and the diameter of the wire was 5–11 µm. The EDS analysis also confirmed the deposition of the successive layers on the entire surface of the microalgae skeleton. For Ni@ZnO@ZnS-*Spirulina,* note that the surface roughness is higher after the sulfidation process (Fig. 1c), which may be beneficial for the adsorption of pollutants and trapping light as a consequence of the improvement in the values of the BET surface area values (Fig. S2a), i.e., 97 $m^2 g^{-1}$ and 129 $m^2 g^{-1}$ for the Ni@ZnO-*Spirulina* and Ni@ZnO@ZnS-*Spirulina* hybrids, respectively. Fig. S2b shows that the XRD pattern of Ni@ZnO-*Spirulina* demonstrated the formation of a polycrystalline ZnO layer, with clear diffraction peaks at 2 θ= 31.79° (100), 34.42° (002), 36.25° (101), 56.60° (110), and 62.86° (103), which are in agreement with wurtzite ZnO (JCPDS card 36–1451) [41–44]. In addition, the formation of a ZnS layer on the previously deposited ZnO, forming the Ni@ZnO@ZnS-Spirulina hybrid, was confirmed by the identification of extra diffraction peaks at 2 θ= 28.55° (111) and 33.87° (200), matching the cubic ZnS blend structure (JCPDS card 65–1691) [41–44]. In both diffraction patterns, a broad peak around 2 θ= 44.5° confirmed the formation of a nanocrystalline Ni coating on the microalgae.

The sedimentation rate also was examined during 10 h period (Fig. S3a) in non-stirring conditions, which is an important property to be considered prior to proposing their usage as photocatalysts since rapid sedimentation can reduce the photocatalytic activity. Fig. S3a shows that the sedimentation was negligible during the first eight hours, but it should be considered for longer times, which is not relevant for photocatalytic applications, such as general magnetic stirring or the application of air bubbling, and, consequently, the sedimentation also is inhibited. Therefore, the ZnO-based hybrids that are prepared can be considered to be lightweight photocatalysts. In addition, Ni@ZnO-*Spirulina* and Ni@ZnO@ZnS-*Spirulina* hybrids exhibit ferromagnetic properties with a rather weak coercivity (Fig. 1d), i.e., the saturation magnetization values are ≈26 emu g^{-1} and ≈25 emu g^{-1}, the remanence is ≈10 emu g^{-1}, and the coercivity is ≈231 Oe for both, Ni@ZnO-*Spirulina* and Ni@ZnO@ZnS-*Spirulina* hybrids, respectively. Importantly, the light weight and magnetic properties of photocatalysts allow them to be manipulated magnetically when they are dispersed in aqueous media. For example, when they are dispersed in a liquid, they can be accumulated and collected easily with an NdFeB magnet (Fig. S3b), which can be important for the improvement of the photocatalytic performance to remove toxic cyanobacteria blooms and cyanotoxins from water.

The optoelectronic properties of ZnO-based hybrids were examined

by using UV–vis DRS (Fig. 1e). It is known that the formation of layered ZnO/ZnS heterojunctions, which are too large for photocatalytic applications using visible light, can reduce the bandgap of ZnO and ZnS drastically. Fig. 1e shows that the absorption edge of the Ni@ZnO@ZnS-*Spirulina* hybrid has a red shift, and the absorption intensities of light in the UV and visible domains were increased in comparison with the Ni@ZnO-*Spirulina* hybrid. Therefore, the formation of the ZnS shell makes the band gap smaller (2.88 ± 0.04 eV) compared to the nude ZnO (3.29 ± 0.05 eV). The bandgap energies were calculated using the Tauc relation (Fig. S4). It is expected that Ni@ZnO@ZnS-*Spirulina* photocatalysts would exhibit a higher photoresponse in the visible region, and, as a result, they had improved photocatalytic activity in response to sunlight irradiation.

3.2. Antimicrobial activity of Ni@ZnO@ZnS hybrid photocatalysts

The photokilling properties of ZnO-based hybrid photocatalysts under the influence of both artificial UV-filtered light irradiation and magnetic actuation (rotatory magnetic field of ~400 Oe at various rotation speeds) were investigated for two different cyanobacteria, namely, *Spirulina platensis paracas* (non-toxic) and (ii) Anabaena *flos-aquae* (toxic), mainly producing anatoxin-A, homoanatoxin-A, and anatoxin-A(s) [35–37]. These filamentous cyanobacteria were selected to (i) analyze the potential of Ni@ZnO@ZnS hybrid photocatalysts for the effective visible-light-driven photokilling of different cyanobacteria blooms and (ii) study the effect of the photocatalyst shape on photocatalyst–microalgae interactions and photokilling activity. Note that *Spirulina platensis paracas* are extended helical microalgae (identical to the photocatalyst shape), whereas Anabaena *flos-aquae* are loose irregularly coiled filaments (Fig. 2a).

Reactor geometry is known to strongly influence heterogeneous catalysis, especially when magnetic components are used, and can reduce catalytic performance as a result of photocatalyst accumulation at points of the strongest magnetic field, which suppresses catalyst-microalgae interactions or hinders light adsorption [45]. Herein, the above effects were probed for two different geometries (Fig. 2b): a vertical geometry using a cylindrical vertical container with a volume of $\pi \times 2^2 \times 30\,cm^3$ and a planar geometry using a cylindrical planar container with a volume of $\pi \times 8^2 \times 6\,cm^3$. The performance of ZnO-based hybrid photocatalysts was investigated by following the reduction of living microalgae content under artificial UV-filtered light irradiation and magnetic actuation in both geometries.

Prior to testing magnetically driven photocatalytic activity, we examined the effects of the following parameters on photocatalyst–microalgae interactions: (i) artificial UV-filtered sunlight irradiation in the absence of the photocatalyst; (ii) magnetic actuation in the absence of the photocatalyst; (iii) microorganism–photocatalyst interaction under the dark conditions without magnetic actuation; and (iv) microorganism–photocatalyst interactions in the dark with magnetic actuation.

As expected, the effects of artificial UV-filtered sunlight irradiation (Fig. S5) and magnetic actuation (Fig. S6) were negligible in the absence of the photocatalyst. In addition, the effect of the photocatalyst on both types of microalgae under both dark and silent (no magnetic actuation) conditions was imperceptible, as Ni@ZnO-*Spirulina* and Ni@ZnO@ZnS-*Spirulina* hybrid photocatalysts did not exhibit biocidal activity (Fig. S7). No differences were observed between the two tested reactor geometries. However, after 80 min of magnetic actuation (400 Oe and 30 Hz) in the dark, the survival rates of *Spirulina* and *Anabaena* microalgae decreased by ~87 and ~95 %, respectively (Fig. S8) when the planar geometry was used. Conversely, the effect of magnetic actuation was negligible when the vertical geometry was used, which was ascribed to photocatalyst accumulation at the bottom of the container, thereby hindering the photocatalyst-microorganism interactions. In turn, the depletion of survival rates was attributed to the mechanical destruction of microalgae skeletons due to the photocatalyst vibration and rotation. Note that the effect was higher for *Spirulina* microalgae, possibly because of their better interaction with the photocatalyst, as both systems had the same shape. Thus, photokilling activity was determined by microorganism species, photocatalyst shape, and reactor geometry.

Ni@ZnO@ZnS-*Spirulina* photocatalysts exhibited the best photokilling ability for both types of microalgae under artificial UV-filtered sunlight irradiation and magnetic actuation, especially when moderate rotation rates (10 Hz) were used (Fig. 2c and d). However, the effect of magnetic actuation was significantly lower when the vertical reactor geometry was used (Fig. S9) as a result of the poor distribution of the photocatalyst in the reaction medium. In addition, photokilling activity was significantly higher under all conditions when the planar geometry was used, as this geometry increased catalyst radiation exposure and thus facilitated light trapping. Consequently, we focused on the planar geometry, in which photokilling activity could be enhanced by applying magnetic actuation.

The higher deactivation of *Spirulina* microalgae compared to that of *Anabaena* was ascribed to the differences in their sizes, morphologies, and shapes. In particular, when the rotation rate of the applied magnetic field was considered, the total elimination of *Spirulina* microalgae was achieved after ~10 min (10 Hz), ~15 min (20 Hz), ~15 min (0 Hz), and ~25 min (30 Hz), while the total elimination of *Anabaena* was attained after ~35 min (10 Hz), ~40 min (0 Hz), ~45 min (20 Hz), and ~60 min (30 Hz). The same trend was observed when Ni@ZnO-*Spirulina* photocatalysts were used (Fig. S10), but the photokilling activity was significantly lower because of the low photoresponse of these catalysts under artificial UV-filtered sunlight. Note that as *Spirulina* microalgae had the same shape as the photocatalysts, we expected improved microalgae-photocatalyst interactions to promote photokilling caused by the formation of reactive oxygen species on the photocatalyst surface cooperatively with the mechanical destruction due to magnetic vibration or rotation. In addition, Ni@ZnO@ZnS-*Spirulina* exhibited excellent reusability under the conditions of UV-filtered sunlight irradiation, magnetic actuation (10 Hz), and planar reactor geometry during eight consecutive 20-min cycles, i.e., the photokilling activity was constant overall (Fig. S11). Therefore, the above photocatalyst may be used to combat harmful microalgae blooms under irradiation with solar visible light.

These results demonstrated that photokilling is mainly related to the formation of reactive oxygen species. Importantly, the microorganism–photocatalyst interaction is an important parameter to consider in photocatalyst design, as this interaction enhances photokilling because of the short lifetime of the reactive oxygen species formed on the photocatalyst surface. In addition, moderate magnetic actuation could synergistically enhance photokilling activity by promoting the mechanical destruction of cell walls; however, high rotation rates negatively affected photokilling activity. In these processes, reactor design strongly influenced the efficiency of light adsorption by the photocatalyst, which is very important in the overall photocatalytic activity, photocatalyst distribution in the reaction medium, and photocatalyst–microorganism interactions. The photokilling mechanism remained unclear, as the viability of microalgae was synergistically affected by multiple parameters (e.g., photocatalyst dissolution and biocidal activity); however, in this case, photocatalyst antimicrobial activity was mainly ascribed to the formation of reactive oxygen species.

To explore the potential of Ni@ZnO@ZnS hybrid microalgae under close to natural conditions we monitored microalgal biomass growth in an 8 L tank containing 0.6 mg L^{-1} of Ni@ZnO@ZnS-*Spirulina* for five days under agitation (mechanical and intermittent) and irradiation (natural sunlight) conditions identical to those used for the cultivation of the microalgae used as templates. Under these conditions, water hindered continuous light adsorption by the photocatalyst, which was not preferentially placed at the water–air interface. Fig. 3 shows that biomass production moderately increased in presence of the

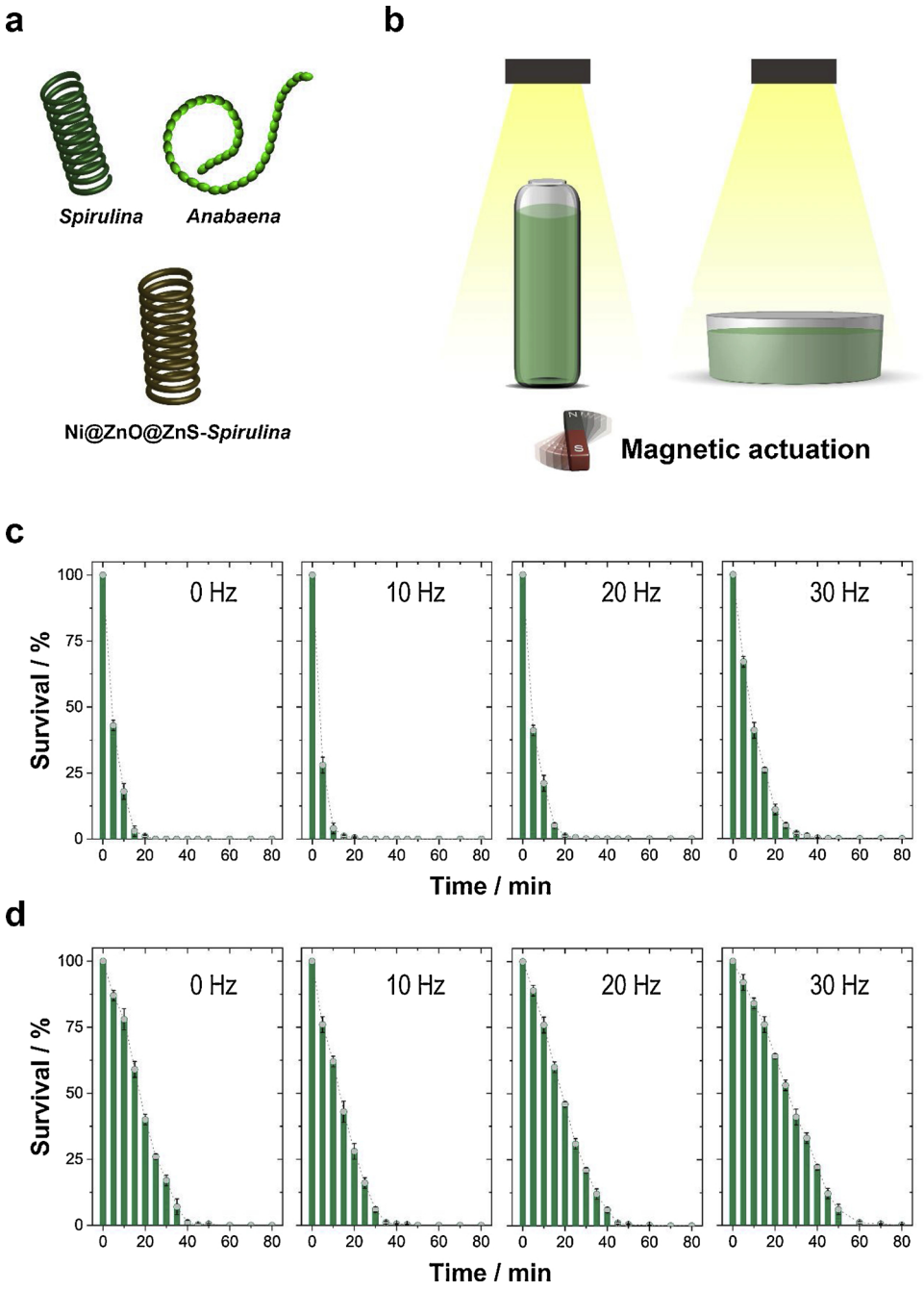

Fig. 2. Schematic representation of (a) *Spirulina platensis paracas*/Anabaena *flos-aquae* cyanobacteria and the Ni@ZnO@ZnS-*Spirulina* photocatalyst and (b) the reactor geometries used in photokilling experiments. Survival rates of (c) *Spirulina platensis paracas* and (d) Anabaena *flos-aquae* under artificial UV-filtered sunlight irradiation and magnetic actuation for the Ni@ZnO@ZnS-*Spirulina* photocatalyst (photocatalyst dosage = 0.6 mg mL^{-1}; temperature = 25 ± 0.2 °C).

photocatalyst during the first two days but strongly decreased subsequently. However, in the absence of the photocatalyst, biomass production continuously increased significantly. Therefore, it is concluded that the Ni@ZnO@ZnS-*Spirulina* photocatalyst can be considered as an effective tool for the elimination of harmful microalgal blooms.

3.3. Photocatalytic activity of Ni@ZnO@ZnS hybrid microalgae

Recently, ZnO-based *Spirulina* hybrid photocatalysts have been effectively used for the mineralization of persistent organic pollutants [41]. To confirm the multi-functional properties of the Ni@ZnO@ZnS-*Spirulina* photocatalyst for the simultaneous elimination of toxic cyanobacteria blooms and cyanotoxins under visible light irradiation, the photomineralization of anatoxin-A was explored.

Blank experiments (without photocatalyst) conducted to consider the photolytic degradation of anatoxin or the effect of magnetic actuation showed that no degradation occurred during 120 min exposure to UV-filtered sunlight irradiation or magnetic actuation (Fig. S12).

The Ni@ZnO@ZnS-*Spirulina* photocatalyst (0.6 mg mL^{-1}) was immersed into a solution containing 5 ppm of (±)-anatoxin-A fumarate in the dark for 90 min to reach the absorption–desorption equilibrium, and the mixture was illuminated with artificial sunlight and subjected to magnetic actuation. Reactor geometry was not considered, as small volumes were used in these experiments. Fig. 4a shows that anatoxin was effectively photodegraded, as evidenced by the significant intensity loss of the time-dependent anatoxin peak in the UHPLC chromatogram

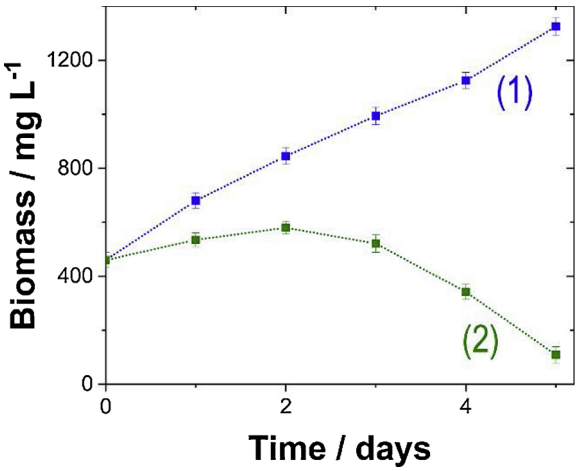

Fig. 3. Production of *Spirulina* biomass in Zarrouk's medium in the absence (1) and presence (2) of the Ni@ZnO@ZnS-*Spirulina* photocatalyst.

during artificial sunlight irradiation. Compared to Ni@ZnO-*Spirulina* (Fig. S13), Ni@ZnO@ZnS-*Spirulina* (Fig. 4b and Table 1) exhibited a significantly higher photocatalytic activity when exposed to artificial sunlight, which was ascribed to the higher photoresponse observed in the visible light domain when the ZnS layer was present. In particular, Ni@ZnO@ZnS-*Spirulina* exhibited the best anatoxin photodegradation activity of 97.4 ± 0.7 %, during moderate magnetic actuation (20 Hz). Figs. 4b, c, and S13 and Table 1 show that moderate magnetic actuation significantly improved photodegradation via enhancing the mass transport of anatoxin molecules to the catalyst surface without affecting the light-trapping capability. Although, the above effect has been reported for heterogeneous catalysis, this is the first time it has been described for hybrid photocatalysts. However, high rotation speeds of the magnetic field negatively affected pollutant adsorption on the photocatalyst surface, as exemplified by the fact that photodegradation increased at rotation speeds of up to 20 Hz but decreased at higher speeds (30 Hz). Magnetic irradiation can improve the mass transport but can negatively affect the adsorption–desorption process of pollutants or the trapping of light. According to the Langmuir–Hinshelwood model, at low concentrations, anatoxin degradation agrees with the pseudo–first order kinetics with respect to pollutant concentration (Fig. S14). Fig. 4c shows that mass-normalized kinetic constants determined in presence of the Ni@ZnO@ZnS-Spirulina photocatalyst under quiescent conditions and in a 400 Oe rotatory magnetic field at 10, 20, and 30 Hz were determined as 10.1, 22.5, 24.2, and 10.3 $min^{-1}\,g^{-1}$, respectively. Fig. 4c clearly shows that moderate rotatory magnetic fields significantly improved the anatoxin photodegradation during artificial sunlight irradiation. The same trend was observed for the Ni@ZnO-Spirulina photocatalyst (Fig. S15), although the corresponding kinetics

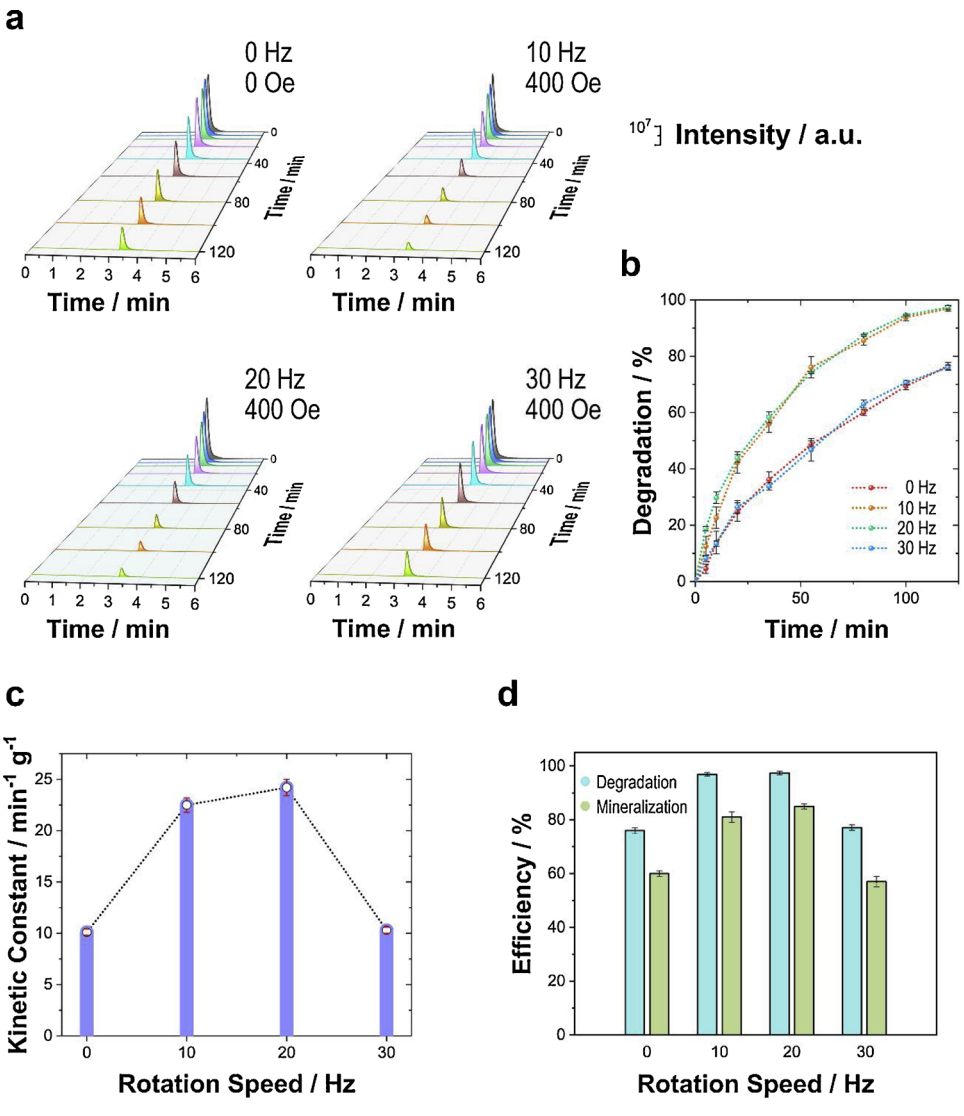

Fig. 4. (a) Time-dependent UHPLC chromatograms and (b) photodegradation efficiency of a 5 ppm solution of (±)-anatoxin-A fumarate containing Ni@ZnO@ZnS-*Spirulina* under artificial sunlight irradiation and magnetic actuation. (c) Mass-normalized kinetic constant of the photodegradation of a 5 ppm solution of (±)-anatoxin-A fumarate containing Ni@ZnO@ZnS-*Spirulina* under artificial sunlight irradiation as a function of the rotation speed of the applied rotatory magnetic field. (d) Degradation and mineralization efficiency of a 5-ppm solution of (±)-anatoxin-A fumarate containing Ni@ZnO@ZnS-*Spirulina* during artificial sunlight irradiation and magnetic actuation. Photocatalyst dosage = 0.6 mg mL^{-1}; temperature = 25 ± 0.2 °C.

Table 1
Photocatalytic degradation and mineralization of 5 ppm (±)-anatoxin-A fumarate solution under artificial sunlight. Photocatalyst dosage = 0.6 mg mL^{-1}; Temperature = 25 ± 0.2 °C.

Photocatalyst	No magnetic actuation			Magnetic actuation		
	0 Hz			10 Hz		
	Photodegradation / %	kinetic constant / $min^{-1} g^{-1}$	Mineralization / %	Photodegradation / %	kinetic constant / $min^{-1} g^{-1}$	Mineralization / %
Ni@ZnO-*Spirulina*	21 ± 3	1.5 ± 0.2	13 ± 2	35 ± 2	2.9 ± 0.3	25 ± 1
Ni@ZnO@ZnS-*Spirulina*	76 ± 1	10.1 ± 0.3	60 ± 1	96.9 ± 0.7	22.5 ± 0.7	81 ± 2
Photocatalyst	Magnetic actuation					
	20 Hz			30 Hz		
	Photodegradation / %	kinetic constant / $min^{-1} g^{-1}$	Mineralization / %	Photodegradation / %	kinetic constant / $min^{-1} g^{-1}$	Mineralization / %
Ni@ZnO-*Spirulina*	40 ± 2	3.6 ± 0.3	31 ± 2	29 ± 2	2.6 ± 0.2	17 ± 2
Ni@ZnO@ZnS-*Spirulina*	97.4 ± 0.7	24.2 ± 0.8	85 ± 1	77 ± 1	10.3 ± 0.3	57 ± 2

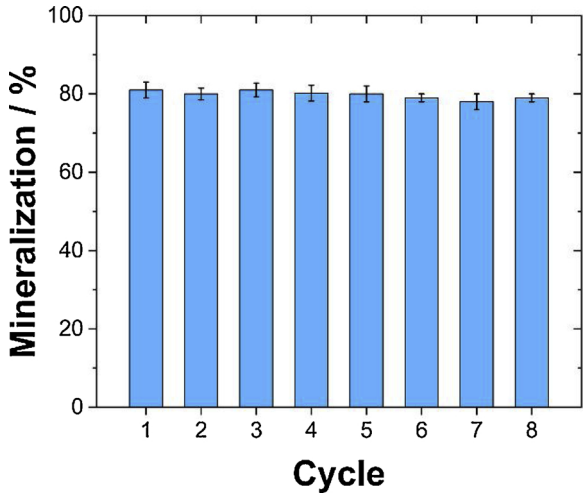

Fig. 5. Effectiveness of the reused Ni@ZnO@ZnS-*Spirulina* photocatalyst for (±)-anatoxin-A fumarate mineralization during artificial sunlight irradiation. Photocatalyst dosage = 0.6 mg mL^{-1}; temperature = 25 ± 0.2 °C.

was much slower because of the lower photoresponse in the visible domain.

The mineralization (i.e., total photooxidation of anatoxin to carbon dioxide) was analyzed by measuring the reduction of the total organic content after irradiation [46,47]. Compared to photodegradation, mineralization was significantly lower, especially for Ni@ZnO-*Spirulina* (Fig. 4d and Table 1), which was explained by the fact that the total photooxidation of anatoxin involved multiple steps. In addition, the application of a rotatory magnetic field had a lower effect on mineralization than the photodegradation, which was ascribed to the fact that the photocatalyst vibration or rotation facilitates the desorption of intermediates that may have been formed during the stages of anatoxin photooxidation.

The reusability of the Ni@ZnO@ZnS-*Spirulina* photocatalyst was evaluated by measuring mineralization during eight consecutive cycles. Fig. 5 shows that the above-mentioned photocatalyst exhibited excellent reusability because of minimal photocorrosion activity. It is known that the formation of a ZnS thin layer on ZnO significantly improves photocorrosion resistance, minimizing the release of Zn(II) into the decontaminated water [41–43]. Importantly, morphological characterization of the reused photocatalyst (Fig. S16) showed that the original architecture and surface were not affected.

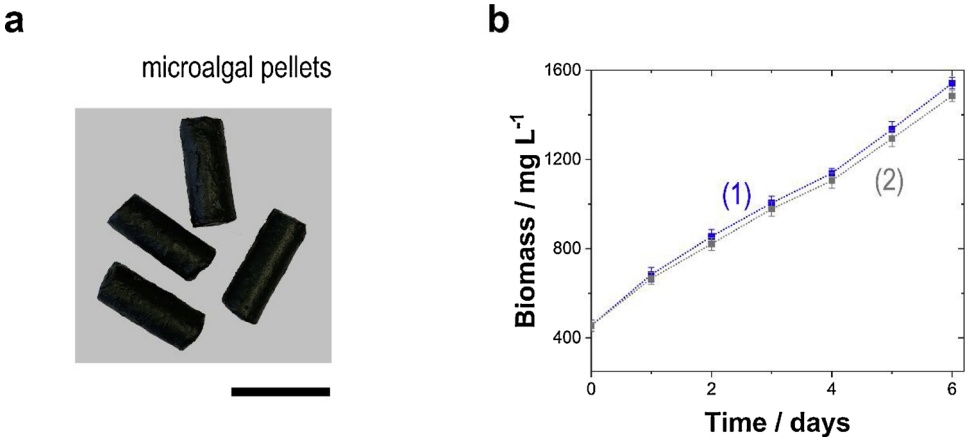

Fig. 6. (a) Photograph of the microalgal pellets manufactured, Scale bar: 2 cm. (b) *Spirulina* biomass production in (1) Zarrouk's medium and (2) microalgal ash-based medium.

3.4. Recyclability of Ni@ZnO@ZnS hybrid microalgae

The aims of green chemistry and circular chemistry are 1) to prevent the production of residues and 2) to increase the efficiency of the use of natural resources, i.e., human capital, energy, and water. Thus, we addressed reinforcing the cleaner production of photocatalysts, recycling them after their effective lifetimes, and explored the fabrication of microalgal pellets. Fig. 6a shows that well-defined, cylindrical pellets ($\pi \times 0.5^2 \times 3\,cm^3$) were manufactured successfully using a single pelletizer. Importantly, the pellets that were obtained satisfied the requirements of the ISO 17225-6:2014 standard for non-woody pellets [48–51], because the ash content was 5.4 ± 0.2 wt. %, the moisture content was 6.8 ± 0.3 wt. %, and the calorific power was 20.1 MJ kg^{-1}. Thus, the microalgal pellets could be proposed as an efficient biofuel for commercialization. It is important to note that microalgal ashes and gases (mainly CO_2) are generated during the combustion of the solid microalgal pellets, but both the ashes and CO_2 can be used to cultivate more microalgal biomass. Thus, the microalgal ashes, which contain nickel and zinc, were used as a supplement of microalgae cultivation media. Importantly, the photocatalytic activity of the obtained ashes after the combustion of these microalgal pellets is zero, thus making it a potential supplement for cultivation of fresh microalgae. Fig. 6b shows that the growth of microalgae biomass was the same when either Zarrouk's medium or the ash-based medium was used, highlighting the additional ability of recycling of the microalgal ashes. The recyclability of the hybrid photocatalysts to produce pellets (i.e., biofuel) and the fact that could replace or supplement the cultivation media of algae (i.e., recycling ashes) inspired the development of a simple, inexpensive circular process based on the cleaner production of effective, multi-functional photocatalysts for photokilling toxic cyanobacteria blooms, with simultaneous mineralization of cyanotoxins, and biofuel production leaving minimal residues.

4. Conclusions

Hybrid magnetic Ni@ZnO@ZnS-*Spirulina* photocatalysts are successfully synthesized by a simple sequential chemical treatment without the modification of the micro-helix algae morphology, leading to the formation of onion-like microstructures with excellent light trapping capability, owing the biomimetic structure and low sedimentation rate under stagnant conditions. The hybrids are effective sunlight-responsive photocatalysts for the removal of algae blooms and the corresponding released toxins. In particular, the Ni@ZnO@ZnS-*Spirulina* photocatalyst shows excellent photokilling activity under UV-filtered sunlight radiation for both types of microalgae (i.e., *Spirulina* and *Anabaena*). However, the deactivation of the microalgae was significantly higher for *Spirulina* microalgae because the photocatalyst–microalgae interaction is favored by mimetic morphology, highlighting the importance of the photocatalyst architecture for efficient interaction with microorganisms. Moderate magnetic rotation rates are attributed to the high photokilling efficiencies. Parallelly, Ni@ZnO@ZnS-*Spirulina* under artificial sunlight exhibited excellent photomineralization activity of anatoxin-A and minimal photocorrosion. Similar to the photokilling process, moderate magnetic actuation significantly improves the photocatalytic performance of anatoxin-A photodegradation. Under magnetic actuation, the reduction of the total organic content owing to mineralization is lower than that due to photodegradation, which may be related to the inauspicious movement effect on the weak adsorption of intermediates, making it stop or slow down the overall degradation process. Importantly, after the photocatalyst lifetime, the hybrids can be recycled by biocombustible formation (i.e. microalgae pellets), after which their combustion generates ashes containing Zn and Ni. The ashes serve as a suitable supplement for the microalgae cultivation media, allowing new *Spirulina* cultivation for biotemplates in a new photocatalyst generation. Consequently, a simple and green circular process with minimal residue production has been proposed for the effective water decontamination, energy production, and microalgae cultivation.

CRediT authorship contribution statement

Albert Serrà: Conceptualization, Methodology, Investigation, Formal analysis, Validation, Writing - original draft, Writing - review & editing. **Petai Pip:** Investigation, Writing - original draft. **Elvira Gómez:** Conceptualization, Validation, Supervision, Writing - review & editing, Funding acquisition. **Laetitia Philippe:** Conceptualization, Validation, Supervision, Writing - review & editing, Funding acquisition.

Declaration of Competing Interest

None.

Acknowledgements

This work was partially supported by the Metrohm foundation. Partial funding from the TEC2017-85059-C3-2-R project (co-financed by the *Fondo Europeo de Desarrollo Regional, FEDER*) from the Spanish *Ministerio de Economía y Competitividad* (MINECO), and the 200020-172774 project from the Swiss National Science Foundation (SNF) is also acknowledged. Albert Serrà would like to acknowledge funding from the EMPAPOSTDOCS-II program. The EMPAPOSTDOCS-II programme has received funding from the European Union's Horizon 2020 research and innovation programme under the Marie Skłodowska-Curie grant agreement number 754364.

Appendix A. Supplementary data

Supplementary material related to this article can be found, in the online version, at doi:https://doi.org/10.1016/j.apcatb.2020.118745.

References

[1] D.G. Schmale, A.P. Ault, W. Saad, D.T. Scott, J.A. Westrick, Perspectives on harmful algal blooms (HABs) and the cyberbiosecurity of freshwater systems, Front. Bioeng. Biotechnol. 7 (2019) 1–7, https://doi.org/10.3389/fbioe.2019.00128.
[2] J. Nimptsch, S. Woelfl, S. Osorio, J. Valenzuela, C. Moreira, V. Ramos, R. Castelo-Branco, P.N. Leão, V. Vasconcelos, First record of toxins associated with cyanobacterial blooms in oligotrophic North Patagonian lakes of Chile- A genomic approach, Int. Rev. Hydrobiol. 101 (2016) 57–68, https://doi.org/10.1002/iroh.201401780.
[3] C.J. Gobler, O.M. Doherty, T.K. Hattenrath-Lehmann, A.W. Griffith, Y. Kang, R.W. Litaker, Ocean warming since 1982 has expanded the niche of toxic algal blooms in the North Atlantic and North Pacific oceans, Proc. Natl. Acad. Sci. U. S. A. 114 (2017) 4975–4980, https://doi.org/10.1073/pnas.1619575114.
[4] C. Christophoridis, S.K. Zervou, K. Manolidi, M. Katsiapi, M. Moustaka-Gouni, T. Kaloudis, T.M. Triantis, A. Hiskia, Occurrence and diversity of cyanotoxins in Greek lakes, Sci. Rep. 8 (2018) 1–22, https://doi.org/10.1038/s41598-018-35428-x.
[5] R.P. Rastogi, D. Madamwar, A. Incharoensakdi, Bloom dynamics of cyanobacteria and their toxins: environmental health impacts and mitigation strategies, Front. Microbiol. 6 (2015) 1–22, https://doi.org/10.3389/fmicb.2015.01254.
[6] A.S. Lorenzi, M.K. Cordeiro-Araújo, M.A. Chia, Mdo C. Bittencourt-Oliveira, Cyanotoxin contamination of semiarid drinking water supply reservoirs, Environ. Earth Sci. 77 (2018), https://doi.org/10.1007/s12665-018-7774-y.
[7] M. Moustaka-Gouni, A. Hiskia, S. Genitsaris, M. Katsiapi, K. Manolidi, S.K. Zervou, C. Christophoridis, T.M. Triantis, T. Kaloudis, S. Orfanidis, First report of Aphanizomenon favaloroi occurrence in Europe associated with saxitoxins and a massive fish kill in Lake Vistonis, Greece, Mar. Freshw. Res. 68 (2017) 793–800, https://doi.org/10.1071/MF16029.
[8] B. Žegura, A. Štraser, M. Filipič, Genotoxicity and potential carcinogenicity of cyanobacterial toxins - a review, Mutat. Res. - Rev. Mutat. Res. 727 (2011) 16–41, https://doi.org/10.1016/j.mrrev.2011.01.002.
[9] D.K. Saini, S. Pabbi, P. Shukla, Cyanobacterial pigments: perspectives and biotechnological approaches, Food Chem. Toxicol. 120 (2018) 616–624, https://doi.org/10.1016/j.fct.2018.08.002.
[10] S. Merel, D. Walker, R. Chicana, S. Snyder, E. Baurès, O. Thomas, State of knowledge and concerns on cyanobacterial blooms and cyanotoxins, Environ. Int. 59 (2013) 303–327, https://doi.org/10.1016/j.envint.2013.06.013.
[11] M.A. Berry, T.W. Davis, R.M. Cory, M.B. Duhaime, T.H. Johengen, G.W. Kling,

J.A. Marino, P.A. Den Uyl, D. Gossiaux, G.J. Dick, V.J. Denef, Cyanobacterial harmful algal blooms are a biological disturbance to Western Lake Erie bacterial communities, Environ. Microbiol. 19 (2017) 1149–1162, https://doi.org/10.1111/1462-2920.13640.

[12] J.M. Clark, B.A. Schaeffer, J.A. Darling, E.A. Urquhart, J.M. Johnston, A.R. Ignatius, M.H. Myer, K.A. Loftin, P.J. Werdell, R.P. Stumpf, Satellite monitoring of cyanobacterial harmful algal bloom frequency in recreational waters and drinking water sources, Ecol. Indic. 80 (2017) 84–95, https://doi.org/10.1016/j.ecolind.2017.04.046.

[13] L.M. Botana, A. Alfonso, Phycotoxins, Chemistry and Biochemistry, John Wiley & Sons, Ltd., United Kingdom, 2015.

[14] S. Corbel, C. Mougin, N. Bouaïcha, Cyanobacterial toxins: modes of actions, fate in aquatic and soil ecosystems, phytotoxicity and bioaccumulation in agricultural crops, Chemosphere 96 (2014) 1–15, https://doi.org/10.1016/j.chemosphere.2013.07.056.

[15] D. Pantelić, Z. Svirčev, J. Simeunović, M. Vidović, I. Trajković, Cyanotoxins: characteristics, production and degradation routes in drinking water treatment with reference to the situation in Serbia, Chemosphere 91 (2013) 421–441, https://doi.org/10.1016/j.chemosphere.2013.01.003.

[16] B.A. Neilan, L.A. Pearson, J. Muenchhoff, M.C. Moffitt, E. Dittmann, Environmental conditions that influence toxin biosynthesis in cyanobacteria, Environ. Microbiol. 15 (2013) 1239–1253, https://doi.org/10.1111/j.1462-2920.2012.02729.x.

[17] S.R. Bickman, K. Campbell, C. Elliott, C. Murphy, R. O'Kennedy, P. Papst, M.J. Lochhead, An innovative portable biosensor system for the rapid detection of freshwater cyanobacterial algal bloom toxins, Environ. Sci. Technol. 52 (2018) 11691–11698, https://doi.org/10.1021/acs.est.8b02769.

[18] F. Edition, Water Quality for Drinking: Who Guidelines, SpringerReference, 2011, https://doi.org/10.1007/springerreference_30502.

[19] Environmental Protection Agency, Drinking Water Health Advisory for the Cyanobacterial Microcystin Toxins, (2015).

[20] Environmental Protection Agency, Drinking Water Health Advisory for the Cyanobacterial Toxin Cylindrospermopsin, (2015).

[21] D.C. Szlag, J.L. Sinclair, B. Southwell, J.A. Westrick, Cyanobacteria and cyanotoxins occurrence and removal from five high-risk conventional treatment drinking water plants, Toxins (Basel). 7 (2015) 2198–2220, https://doi.org/10.3390/toxins7062198.

[22] M. Munoz, J. Nieto-Sandoval, S. Cirés, Z.M. de Pedro, A. Quesada, J.A. Casas, Degradation of widespread cyanotoxins with high impact in drinking water (microcystins, cylindrospermopsin, anatoxin-a and saxitoxin) by CWPO, Water Res. 163 (2019), https://doi.org/10.1016/j.watres.2019.114853.

[23] J. Bialczyk, P. Natkański, P. Kuśtrowski, U. Czaja-Prokop, B. Bober, A. Kaminski, Removal of cyanobacterial anatoxin-a from water by natural clay adsorbents, Appl. Clay Sci. 148 (2017) 17–24, https://doi.org/10.1016/j.clay.2017.07.026.

[24] S. Vlad, W.B. Anderson, S. Peldszus, P.M. Huck, Removal of the cyanotoxin anatoxin-a by drinking water treatment processes: a review, J. Water Health 12 (2014) 601–617, https://doi.org/10.2166/wh.2014.018.

[25] S. Chae, T. Noeiaghaei, Y. Oh, I.S. Kim, J.S. Park, Effective removal of emerging dissolved cyanotoxins from water using hybrid photocatalytic composites, Water Res. 149 (2019) 421–431, https://doi.org/10.1016/j.watres.2018.11.016.

[26] J.A. Park, B. Yang, M. Jang, J.H. Kim, S.B. Kim, H.D. Park, H.M. Park, S.H. Lee, J.W. Choi, Oxidation and molecular properties of microcystin-LR, microcystin-RR and anatoxin-a using UV-light-emitting diodes at 255 nm in combination with H_2O_2, Chem. Eng. J. 366 (2019) 423–432, https://doi.org/10.1016/j.cej.2019.02.101.

[27] M.G. Antoniou, P.A. Nicolaou, J.A. Shoemaker, A.A. de la Cruz, D.D. Dionysiou, Impact of the morphological properties of thin TiO2 photocatalytic films on the detoxification of water contaminated with the cyanotoxin, microcystin-LR, Appl. Catal. B Environ. 91 (2009) 165–173, https://doi.org/10.1016/j.apcatb.2009.05.020.

[28] G. Zhang, Y.C. Zhang, M. Nadagouda, C. Han, K. O'Shea, S.M. El-Sheikh, A.A. Ismail, D.D. Dionysiou, Visible light-sensitized S, N and C co-doped polymorphic TiO2 for photocatalytic destruction of microcystin-LR, Appl. Catal. B Environ. 144 (2014) 614–621, https://doi.org/10.1016/j.apcatb.2013.07.058.

[29] Y. Cui, C. Yang, S. Tang, Y. Zhao, F. Chen, Two dimension C_3N_4 /MoS2 nanocomposites with enhanced photocatalytic hydrogen evolution under visible light irradiation, J. Wuhan Univ. Technol. Mater. Sci. Ed. 34 (2019) 23–29, https://doi.org/10.1007/s11595-019-2009-y.

[30] G. Li, X. Nie, J. Chen, Q. Jiang, T. An, P.K. Wong, H. Zhang, H. Zhao, H. Yamashita, Enhanced visible-light-driven photocatalytic inactivation of Escherichia coli using g-C_3N_4/TiO_2 hybrid photocatalyst synthesized using a hydrothermal-calcination approach, Water Res. 86 (2015) 17–24, https://doi.org/10.1016/j.watres.2015.05.053.

[31] W. Wang, G. Li, D. Xia, T. An, H. Zhao, P.K. Wong, Photocatalytic nanomaterials for solar-driven bacterial inactivation: recent progress and challenges, Environ. Sci. Nano 4 (2017) 782–799, https://doi.org/10.1039/C7EN00063D.

[32] D.C. Ducat, J.C. Way, P.A. Silver, Engineering cyanobacteria to generate high-value products, Trends Biotechnol. 29 (2011) 95–103, https://doi.org/10.1016/j.tibtech.2010.12.003.

[33] P.D. Karkos, S.C. Leong, C.D. Karkos, N. Sivaji, D.A. Assimakopoulos, Spirulina in clinical practice: evidence-based human applications, Evidence-Based Complement, Altern. Med. 2011 (2011), https://doi.org/10.1093/ecam/nen058.

[34] A.L. Lupatini, L.M. Colla, C. Canan, E. Colla, Potential application of microalga Spirulina platensis as a protein source, J. Sci. Food Agric. 97 (2017) 724–732, https://doi.org/10.1002/jsfa.7987.

[35] S. Matsunaga, R.E. Moore, W.P. Niemczura, W.W. Carmichael, Anatoxin-a(s), a potent anticholinesterase from Anabaena flos-aquae, J. Am. Chem. Soc. 111 (1989) 8021–8023, https://doi.org/10.1021/ja00202a057.

[36] N.A. Mahmood, W.W. Carmichael, Anatoxin-a(s), an anticholinesterase from the cyanobacterium Anabaena flos-aquae NRC-525-17, Toxicon. 25 (1987) 1221–1227, https://doi.org/10.1016/0041-0101(87)90140-1.

[37] Z.Y. Qian, J. Ma, C. lei Sun, Z.G. Li, Q.M. Xian, T.T. Gong, B. Xu, Using stable isotope labeling to study the nitrogen metabolism in Anabaena flos-aquae growth and anatoxin biosynthesis, Water Res. 127 (2017) 223–229, https://doi.org/10.1016/j.watres.2017.09.060.

[38] X. Li, H. Zhao, C. Liu, J. Cai, Y. Zhang, Y. Jiang, D. Zhang, High-efficiency alignment of 3D biotemplated helices via rotating magnetic field for terahertz chiral metamaterials, Adv. Opt. Mater. 7 (2019) 1–13, https://doi.org/10.1002/adom.201900247.

[39] X. Tao, R. Wu, Y. Xia, H. Huang, W. Chai, T. Feng, Y. Gan, W. Zhang, Biotemplated fabrication of Sn@C anode materials based on the unique metal biosorption behavior of microalgae, ACS Appl. Mater. Interfaces 6 (2014) 3696–3702, https://doi.org/10.1021/am500020e.

[40] K. Kamata, Z. Piao, S. Suzuki, T. Fujimori, W. Tajiri, K. Nagai, T. Iyoda, A. Yamada, T. Hayakawa, M. Ishiwara, S. Horaguchi, A. Belay, T. Tanaka, K. Takano, M. Hangyo, Spirulina-templated metal microcoils with controlled helical structures for THz electromagnetic responses, Sci. Rep. 4 (2014) 1–7, https://doi.org/10.1038/srep04919.

[41] A. Serrà, R. Artal, J. García-Amorós, B. Sepúlveda, E. Gómez, J. Nogués, L. Philippe, Hybrid Ni@ZnO@ZnS-Microalgae for circular economy: a smart route to the efficient integration of solar photocatalytic water decontamination and bioethanol production, Adv. Sci. 7 (2020) 1902447, https://doi.org/10.1002/advs.201902447.

[42] A. Serrà, Y. Zhang, B. Sepúlveda, E. Gómez, J. Nogués, J. Michler, L. Philippe, Highly active ZnO-based biomimetic fern-like microleaves for photocatalytic water decontamination using sunlight, Appl. Catal. B Environ. 248 (2019) 129–146, https://doi.org/10.1016/j.apcatb.2019.02.017.

[43] A. Serrà, Y. Zhang, B. Sepúlveda, E. Gómez, J. Nogués, J. Michler, L. Philippe, Highly reduced ecotoxicity of ZnO-based micro/nanostructures on aquatic biota: influence of architecture, chemical composition, fixation, and photocatalytic efficiency, Water Res. 169 (2020), https://doi.org/10.1016/j.watres.2019.115210.

[44] K.S. Ranjith, R.B. Castillo, M. Sillanpaa, R.T. Rajendra Kumar, Effective shell wall thickness of vertically aligned ZnO-ZnS core-shell nanorod arrays on visible photocatalytic and photo sensing properties, Appl. Catal. B Environ. 237 (2018) 128–139, https://doi.org/10.1016/j.apcatb.2018.03.099.

[45] A. Serrà, S. Grau, C. Gimbert-Suriñach, J. Sort, J. Nogués, E. Vallés, Magnetically-actuated mesoporous nanowires for enhanced heterogeneous catalysis, Appl. Catal. B Environ. 217 (2017) 81–91, https://doi.org/10.1016/j.apcatb.2017.05.071.

[46] Z. Wei, F. Liang, Y. Liu, W. Luo, J. Wang, W. Yao, Y. Zhu, Photoelectrocatalytic degradation of phenol-containing wastewater by TiO2/g-C3N4 hybrid heterostructure thin film, Appl. Catal. B Environ. 201 (2017) 600–606, https://doi.org/10.1016/j.apcatb.2016.09.003.

[47] X. Liu, D. Yang, Y. Zhou, J. Zhang, L. Luo, S. Meng, S. Chen, M. Tan, Z. Li, L. Tang, Electrocatalytic properties of N-doped graphite felt in electro-Fenton process and degradation mechanism of levofloxacin, Chemosphere 182 (2017) 306–315, https://doi.org/10.1016/j.chemosphere.2017.05.035.

[48] M. Barbanera, E. Lascaro, V. Stanzione, A. Esposito, R. Altieri, M. Bufacchi, Characterization of pellets from mixing olive pomace and olive tree pruning, Renew. Energy 88 (2016) 185–191, https://doi.org/10.1016/j.renene.2015.11.037.

[49] E.R. Widjaya, G. Chen, L. Bowtell, C. Hills, Gasification of non-woody biomass: a literature review, Renew. Sustain. Energy Rev. 89 (2018) 184–193, https://doi.org/10.1016/j.rser.2018.03.023.

[50] B. Jagustyn, M. Kmieć, Ł. Smędowski, M. Sajdak, The content and emission factors of heavy metals in biomass used for energy purposes in the context of the requirements of international standards, J. Energy Inst. 90 (2017) 704–714, https://doi.org/10.1016/j.joei.2016.07.007.

[51] I.M. Ríos-Badrán, I. Luzardo-Ocampo, J.F. García-Trejo, J. Santos-Cruz, C. Gutiérrez-Antonio, Production and characterization of fuel pellets from rice husk and wheat straw, Renew. Energy 145 (2020) 500–507, https://doi.org/10.1016/j.renene.2019.06.048.